atmosphere

MDPI

Article

Estimation and Compensation of the Ionospheric Path Delay Phase in PALSAR-3 and NISAR-L Interferograms

Urs Wegmüller *, Charles Werner, Othmar Frey and Christophe Magnard

Gamma Remote Sensing AG, Worbstrasse 225, CH-3073 Gümligen, Switzerland
* Correspondence: wegmuller@gamma-rs.ch; Tel.: +41-31-9517005

Abstract: Spatial and temporal variation in the free electron concentration in the ionosphere affects SAR interferograms, in particular at low radar frequencies. In this work, the identification, estimation, and compensation of ionospheric path delay phases in PALSAR-3 and NISAR-L interferograms are discussed. Both of these L-band sensors simultaneously acquire SAR data in a main spectral band and in an additional, spectrally separated, narrower second band to support the mitigation of ionospheric path delays. The methods presented permit separating the dispersive and the non-dispersive phase terms based on the double-difference interferogram between the two available spectral bands and the differential interferogram of the main band. The applicability of the proposed methods is demonstrated using PALSAR-3-like data that were simulated based on PALSAR-2 SM1 mode data.

Keywords: SAR; interferometry; ionospheric path delay; dispersive phase; non-dispersive phase; split-spectrum; PALSAR-3; NISAR

Citation: Wegmüller, U.; Werner, C.; Frey, O.; Magnard, C. Estimation and Compensation of the Ionospheric Path Delay Phase in PALSAR-3 and NISAR-L Interferograms. *Atmosphere* **2024**, *15*, 632. https://doi.org/10.3390/atmos15060632

Academic Editors: Qiong Tang and Yi Liu

Received: 25 April 2024
Revised: 16 May 2024
Accepted: 22 May 2024
Published: 24 May 2024

Copyright: © 2024 by the authors. Licensee MDPI, Basel, Switzerland. This article is an open access article distributed under the terms and conditions of the Creative Commons Attribution (CC BY) license (https://creativecommons.org/licenses/by/4.0/).

1. Introduction

In 2024, JAXA and NASA plan to launch their L-band SAR instruments PALSAR-3 [1] and NISAR-L [2]. PALSAR-3 is the successor of the successful Japanese L-band SAR missions PALSAR (2006–2010) and PALSAR-2 (launch in 2014, operation still ongoing in 2024). NISAR-L is the L-band SAR element of the NASA-ISRO Synthetic Aperture Radar Mission NISAR. Both missions plan to acquire large volumes of high-resolution data with the expectation of advancing the use of satellite SAR remote sensing, and in particular interferometric SAR applications.

SAR interferometry [3,4] has been successfully used for over 20 years to create numerical elevation models [5] and to map terrain displacement, including seismic motion [6,7], volcano deformation [8], and motion of landslides [9–11] and ice [12–14]. The interferometric phase not only contains information about ground geometry and displacement, but also is influenced by changes in the troposphere and ionosphere [15]. Satellite-based SAR systems are generally located at altitudes above 500 km, i.e., above a significant part of the ionosphere. The interferometric SAR phase can be expressed as a sum of phase components. These are the orbital phase, the topographic phase, the deformation phase, and the differential tropospheric path delay phase. All of these are linearly dependent on the radar frequency. The ionospheric phase shift (in radians), or ionospheric phase for short, on the other hand, is dispersive and inversely proportional to the frequency [16]

$$\phi_{iono} = \frac{4\pi K}{c f_0} \Delta TEC \quad (1)$$

where ΔTEC is the difference between the Total Electron Content (TEC) values integrated along the line-of-sight of the two radar acquisitions, and $K = 40.31$ m^{3}s^{-2} is a constant, c is the speed of light, and f_0 is the radar center frequency. In this work on the identification

and mitigation of ionospheric effects, we do not call the dispersive phase, i.e., the phase term proportional to $1/f_0$, "ionosphere phase" or "ionospheric path delay phase", as SAR data focusing using imperfect parameters is another possible cause for dispersive phase. Using a slightly wrong Doppler rate can result in an overall dispersive phase ramp.

The concept of the split-spectrum approach is to determine separate interferograms for spectral sub-bands, permitting the separation of the dispersive and the non-dispersive phase terms [16–25]. As compared to previous sensors, PALSAR-3 [1] and NISAR-L [2] provide data in two separated spectral bands, a broader main spectral band, and a narrower secondary spectral band. This is specifically to facilitate the estimation of the dispersive phase component. In preparation of the ionosphere mitigation in PALSAR-3 and NISAR-L data, the motivation of our work is to extend the mitigation techniques to SAR data with two separate frequency bands and test them using 80 MHz bandwidth PALSAR-2 SM1 mode data filtered to simulate the dual-band data expected from PALSAR-3 and NISAR-L.

In Section 2, we first present the data used and then generalize the spectral diversity method so that it can be applied for both the single-band and dual-band cases. Furthermore, we also consider the method proposed in [26], namely, to express the dispersive and non-dispersive phases as a linear combination of the main interferogram phase and the double-difference interferogram phase, as this has significant advantages concerning the robustness and accuracy of the method. In Section 3, some processing related aspects are discussed, followed by a discussion of the results obtained using simulated PALSAR-3 data and conclusions.

2. Materials and Methods

2.1. Simulation of PALSAR-3 Single-Look Complex (SLC) Data with Two Spectral Bands Based on PALSAR-2 SM1 Mode SLC Data

Using an interferometric pair of PALSAR-2 SM1 data over Osaka with a bandwidth of 80 MHz, we simulated PALSAR-3 data with the characteristics shown in Table 1. First, we filtered the PALSAR-2 SM1 data with 28 MHz and 10 MHz bandpass filters at the low and high ends of the available 80 MHz chirp bandwidth. Next, we moved the range spectra of the filtered sub-bands to the center of the spectrum. This step corresponds to a change in the center frequency of the data set and was realized by subtracting a phase ramp in the range direction. This provided us one SLC per filtered sub-band, but still in the geometry of the original 80 MHz SLC, which means with a signal bandwidth significantly smaller than the sampling bandwidth. To increase the signal bandwidth to 80% of the sampling bandwidth, we reduced the sampling bandwidth by resampling the data to a coarser range resolution. The metadata are then also updated with the modified center frequency and range sampling values. As a result, simulated SLCs were obtained that correspond to the PALSAR-3 bands of 28 MHz and 10 MHz.

Table 1. Factors a, b, c, d, x, and z used in Equations (3)–(6) to calculate the dispersive and non-dispersive phase components for different PALSAR-1, PALSAR-2, PALSAR-3, and NISAR-L modes. The center frequencies used in the calculations are indicated.

Mode	f_0[GHz]	f_L[GHz]	f_H[GHz]	a	b	c	d	x	z
PALSAR-3 28 MHz	1.2330	1.2330	1.2910	11.38	−10.87	−10.39	10.87	0.511	−10.87
NISAR L 20 MHz	1.2275	1.2275	1.2950	9.85	−9.34	−8.85	9.34	0.513	−9.34
NISAR L 40 MHz	1.2375	1.2375	1.2950	11.52	−11.01	−10.52	11.01	0.511	−11.01
PALSAR-1 14 MHz	1.2700	1.2653	1.2747	68.24	−67.74	−67.74	68.24	0.500	−67.99
PALSAR-1 28 MHz	1.2700	1.2607	1.2793	34.28	−33.78	−33.78	34.28	0.500	−34.03
PALSAR-2 12 MHz	1.2365	1.2325	1.2405	78.17	−77.67	−77.67	78.17	0.500	−77.92
PALSAR-2 25 MHz	1.2700	1.2617	1.2783	38.50	−38.00	−38.00	38.50	0.500	−38.25
PALSAR-2 80 MHz	1.2575	1.2310	1.2840	12.12	−11.62	−11.62	12.12	0.500	−11.88

2.2. Adapting the Split-Spectrum Method to the PALSAR-3 and NISAR L-Band SAR Cases

In the split-spectrum approach, at least two separate spectral bands are used. We name the corresponding center frequencies f_L for the lower- and f_H higher-frequency band. In addition, we use a third frequency f_0 for the center frequency of the main frequency band; this is the frequency band of the interferometric analysis that is conducted after the estimation and mitigation of the ionospheric phase. In the case of data with a single frequency band, f_0 is typically the center frequency of the full frequency band. In the case of data with two separate frequency bands, f_0 is the frequency of the main (broader) frequency band, which can be the lower- or higher-frequency band.

In our derivation, the interferogram phases at frequencies f_0, f_L, and f_H are called ϕ_0, ϕ_L, and ϕ_H, and the related dispersive and non-dispersive components $\phi_{iono,0}$, $\phi_{iono,L}$, $\phi_{iono,H}$, $\phi_{nd,0}$, $\phi_{nd,L}$, and $\phi_{nd,H}$. Considering the indirect and direct proportionality of the dispersive and non-dispersive phase terms, we can write the following set of equations:

$$\begin{aligned} \phi_0 &= \phi_{iono,0} + \phi_{nd,0} \\ \phi_L &= \phi_{iono,0}\frac{f_0}{f_L} + \phi_{nd,0}\frac{f_L}{f_0} \\ \phi_H &= \phi_{iono,0}\frac{f_0}{f_H} + \phi_{nd,0}\frac{f_H}{f_0} \ . \end{aligned} \tag{2}$$

Equation (2) can be transformed to express the dispersive and non-dispersive phase terms as linear combinations of ϕ_L and ϕ_H:

$$\phi_{iono,0} = a\phi_L + b\phi_H \ \text{ with } a = \frac{f_L f_H^2}{f_0(f_H^2 - f_L^2)} \text{ and } b = -\frac{f_L^2 f_H}{f_0(f_H^2 - f_L^2)} \tag{3}$$

$$\phi_{nd,0} = c\phi_L + d\phi_H \quad \text{with } c = -\frac{f_0 f_L}{(f_H^2 - f_L^2)} \text{ and } d = \frac{f_0 f_H}{(f_H^2 - f_L^2)} \ , \tag{4}$$

or as a linear combination of ϕ_0 and $(\phi_H - \phi_L)$:

$$\begin{aligned} \phi_{iono,0} &= x\phi_0 + z(\phi_H - \phi_L) \text{ with } x = \frac{f_H - f_L}{\left(\frac{f_0^2}{f_H} - \frac{f_0^2}{f_L}\right) - (f_H - f_L)} \\ \text{And} \qquad z &= \frac{f_0}{\left(\frac{f_0^2}{f_H} - \frac{f_0^2}{f_L}\right) - (f_H - f_L)} \end{aligned} \tag{5}$$

$$\phi_{nd,0} = (1 - x)\phi_0 - z(\phi_H - \phi_L) \tag{6}$$

with x and z as in Equation (5).

For data with a single spectral band, a quite common approach is to calculate spectral bands for the highest and lowest third of the processed chirp spectrum. For specific PALSAR-1 and PALSAR-2, PALSAR-3, and NISAR modes, the resulting scaling factors are listed in Table 1. For PALSAR-1 and PALSAR-2 modes, center frequencies of specific data we have access to are used. For PALSAR-3, the characteristics used were found in [1], and those for NISAR-L in [2].

Factors a, b, c, and d are used to scale the phases of the differential interferograms in the lower and upper spectral band. To perform phase scaling with a non-integer factor, it is necessary for this phase to have already been unwrapped. As can be seen from Table 1, factors a, b, c, and d are non-integer values that are significantly greater than 1. This is problematic as it upscales phase noise and phase errors from the spatial filtering applied to reduce noise and facilitate phase unwrapping.

Using Equations (3) and (4) requires scaling of the unwrapped phases with large factors. Even small phase errors or noise effects of 0.1 radian will be scaled up, resulting in

significant phase errors. Assuming similar uncertainties for ϕ_L and ϕ_H and considering that factors a, b are quite similar results in an $\phi_{iono,0}$ uncertainty of about square root of 2 times a times the uncertainties for ϕ_L. Using Equations (5) and (6), instead, significantly reduces the scaling of the uncertainties thanks to a much smaller factor x. Furthermore, the double-difference interferogram scaled with factor z is easier to unwrap, which tends to reduce its uncertainty. Therefore, using Equations (5) and (6), i.e., the approach based on the main band interferogram phase and the double-difference interferogram between the lower and higher spectral bands is preferred, as it makes the ionosphere mitigation more robust and accurate [26].

For new sensors with an additional secondary frequency band (PALSAR-3, NISAR-L), the separation of the main and secondary frequency band is relatively large. The resulting factors z between 9 and 12, used to scale the unwrapped differential interferometric phase, are much smaller than in the case of a single frequency band, except for the 80MHz bandwidth PALSAR-2 SM1 mode data. The scaling of the split-spectrum double-difference phase with factor z, which has comparable values to factors a and b, is less critical. The phase is usually much smaller than a phase cycle, so that unwrapping becomes trivial. Strong spatial filtering to perform the unwrapping is therefore not necessary.

In all the investigated cases, the scale factor for the phase of the differential interferogram of the main band, x, has values very close to 0.5. The relative deviations of x from 0.5 are <3%, so replacing it with 0.50 results in scaling errors below 3%. Approximating x with 0.5 and multiplying both sides of Equation (5) by 2 results in

$$2\phi_{iono,0} = \phi_0 + 2z(\phi_H - \phi_L) \ . \tag{7}$$

In contrast to Equation (5), Equation (7) can also be applied to the complex-valued differential interferogram phase ϕ_0, since no scaling of ϕ_0 with a non-integer value is necessary. This means that we can determine a complex-valued image for twice the dispersive phase and only need to unwrap the double-differential interferogram, which can be achieved by directly converting the complex values into phase values. On the one hand, this complex-valued image makes it possible to qualitatively determine the extent of the ionospheric effects. On the other hand, it can be unwrapped to quantify the relative ionospheric phase delays. For pairs with small ionospheric effects, which should be the vast majority of interferometric pairs, unwrapping $2\phi_{iono,0}$ should not be too difficult. In many cases, the phases will remain in the interval $[-\pi,\pi]$, with respect to a reference near the center of the image, or they will vary along an almost linear phase ramp.

A complex-valued image of twice the non-dispersive phase can be calculated by subtracting twice the dispersive phase from twice the interferogram phase. Inserting twice the dispersive phase as expressed in Equation (7) results in

$$2\phi_{non-dispersive,0} = 2\phi_0 - 2\phi_{iono,0} = \phi_0 - 2z(\phi_H - \phi_L) \ . \tag{8}$$

This means a complex version of twice the non-dispersive phase, or the "ionosphere-corrected" interferogram, can be generated without the need for phase unwrapping of the complex-valued differential interferogram ϕ_0.

The main non-dispersive phase terms are deformation phase and tropospheric path delay phase, considering that orbital and topographic phase terms are usually modeled and subtracted. In addition, there are error terms and phase noise.

Very often, and especially in L-band, the spatial variation of the non-dispersive phase is rather small. In cases with strong ionospheric phase effects, unwrapping the double non-dispersive phase can be much easier than unwrapping the original interferogram. An example where the dispersive phase is significantly larger than the non-dispersive phase is presented below. Cases with strong non-dispersive phases occur at displacements of more than one decimeter, caused for example by earthquakes, ice movements, and rapid landslides, and subsidence.

In the following sections, we call the method based on Equation (5) Method 1 (M1). The dispersive phase of the main frequency band is calculated based on the unwrapped

split-spectrum double-difference phase and the unwrapped phase of the differential interferogram. The great advantage of M1 is that the unwrapped phase is only scaled by a small factor of about 0.5, which greatly reduces the quality requirements regarding filtering. M1 does not require an approximation and uses exact scaling factors. The non-dispersive phase of the main frequency band is then either calculated using Equation (6), which provides directly the unwrapped non-dispersive phase, or the unwrapped dispersive phase is subtracted from the complex-valued differential interferogram of the main band to obtain the complex-valued "ionosphere-corrected" differential interferogram.

The methods based on Equations (7) and (8) are called Methods 2 and 3 (M2, M3). The obvious advantage of M2 and M3 is that complex-valued images of twice the dispersive phase (M2) and twice the non-dispersive phase (M3) can be calculated, whereby only the split-spectrum double-difference phase has to be unwrapped. As already mentioned, this step is straightforward. Provided that the double dispersive phase or the double non-dispersive phase can be unwrapped, scaling is also possible to obtain the unwrapped dispersive and non-dispersive phases. It is helpful that often either the double dispersive phase or the double non-dispersive phase have only small values and are therefore easy to unwrap. As M2 and M3 use the same phase terms, we typically apply both methods.

2.3. Processing-Related Aspects

2.3.1. Band-Pass Filtering

When using SLC data in a single frequency band, band-pass filtering along the range spectrum axis, e.g., considering the lowest and highest third of the processed bandwidth, is applied to obtain two sub-band SLCs in a lower and higher spectral bands. Here, in the case of simulated PALSAR-3 or NISAR-L data, we consider SLC data sets that are already provided in two bands, a main band with a typically broader range bandwidth (e.g., 28 MHz in the case of PALSAR-3) and a secondary narrower band (10 MHz in the PALSAR-3 case). Consequently, no band-pass filtering is necessary in the mitigation of the dispersive phase.

2.3.2. Effects of the SLC Co-Registration on the Interferogram

Gradients in the dispersive path delay along the synthetic aperture lead to azimuthal position deviations [27], which can be up to several SLC pixels for L-band images (see example below). If using a co-registration method that is either based exclusively on the orbit data, the SAR processing parameters, and a digital elevation model (DEM), or a method that is based on range and azimuth offset polynomials of low order, which are determined with the aid of matching techniques, an appropriate co-registration is obtained overall. However, local effects caused by the dispersion path delay gradients are not compensated. Registration errors larger than one pixel lead to a significant reduction in coherence. In addition, we have found that registration errors can also significantly affect the interferogram phase, as demonstrated by the example presented in Section 4.

Our co-registration procedure, which also includes a consideration of local effects, comprises a first step based on the orbit, the SAR parameters, and a DEM, and a second step in which the remaining local offsets are determined using matching techniques. Taking into account the quality of the determined offsets and their spatial consistency, the offset field is conditioned. Outliers are removed and the offset field is interpolated in areas with poor coverage and then slightly spatially filtered. The resulting offset field is then used to refine the co-registration.

An iteration of this procedure or the use of the split-beam double-difference phase may not be successful in the case of strong ionospheric gradients. Different parts of the azimuth spectrum of the SLC are affected by different parts of the ionosphere (as the relevant layer is located at a height of almost 300 km above ground and is not on or near the ground).

Applying the co-registration with the offset field refinement results in a much-reduced split-beam interferogram (SBI) phase. But in areas with really high gradients, there

may still be a non-zero SBI phase and further refining the co-registration will also not fully correct this.

Conducting the same co-registration procedure with offset field refinements per azimuth sub-band and combining then the co-registered azimuth sub-band SLCs again into one full-band SLC results in an SBI with significant non-zero "ionosphere-like" phase streaks.

2.3.3. Interferogram Filtering and Unwrapping

Multi-looking and spatial filtering are used to reduce phase noise in interferograms and to support the necessary phase unwrapping step. Spatial filtering also allows the phase signal to be interpolated for small gaps, e.g., in areas with low coherence. Spatial filtering methods exist for both complex-valued and real-valued data sets. A commonly used method for filtering complex-valued interferograms is the Goldstein–Werner filter [28]. We use a modified version of it, which is available in the Gamma software [29]. We usually filter unwrapped phase images with a moving window filter with different filter sizes and weighting functions. For spatial phase unwrapping, we use a minimum cost flow (MCF) algorithm [30], where the interferometric coherence is taken into account in the calculation of the cost function [29].

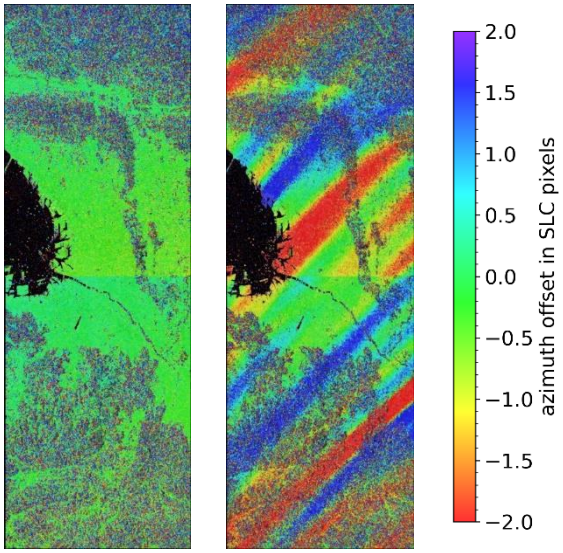
It is also possible to iterate the phase unwrapping procedure, e.g., for interferograms with very large phase signals. An initial solution is generated using a stronger filter. It is important that the unwrapped phase does not show any phase jumps. This first solution is then subtracted from the original interferogram. The resulting complex-valued interferogram has less phase variation than the original interferogram. By repeating the filtering, unwrapping, and subtracting, the phase variation in the remaining complex-valued interferogram can be further reduced. As soon as the phase variation remains within the interval $(-\pi,\pi)$, the complex-valued interferogram can be converted directly into a real-valued phase image. The unwrapped phase is then obtained by summing up the components from the individual iteration steps.

3. Results Using Simulated PALSAR-3 Data over Osaka

Using an interferometric pair of PALSAR-2 SM1 data over Osaka, with 80 MHz bandwidth, we simulated PALSAR-3 data with the characteristics as indicated in Table 1. Two subsequent scenes were concatenated to obtain a better spatial coverage of the ionospheric distortions present. The concatenation was performed after the range band-pass filtering.

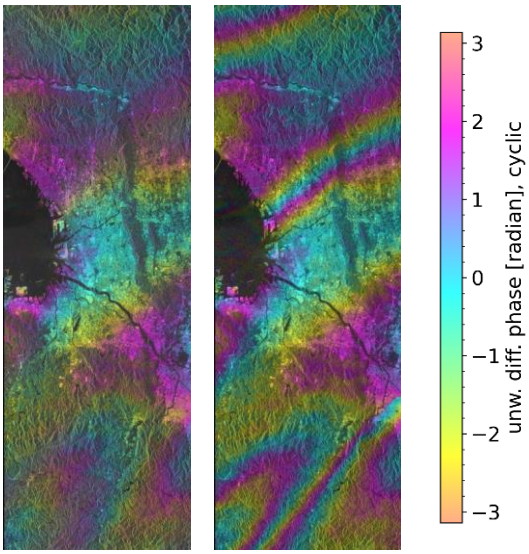
For the main band SLCs, we conducted an ionosphere check for the single SLC by determining the offset field between azimuth sub-band images (Figure 1). Pixel-level azimuth offsets clearly identified the scene acquired on 20160601 as significantly affected by ionospheric effects.

For interferometric processing, we used the earlier scene, i.e., the one without strong ionospheric effects, as the geometric reference. For comparison, we carried out the co-registration with and without an offset field refinement. The resulting differential interferograms are quite different (Figure 2). Differential interferograms calculated for smaller azimuth sub-bands look quite similar to the differential interferogram obtained with the co-registration with an offset field refinement. But the location of the strong phase gradients, which correspond to the location of the dispersive path delay gradients, differs depending on the squint angle of the selected azimuth sub-band, as the ionospheric effects occur at a significant height (e.g., 300 km) above the ground surface. Summing up, the azimuth sub-band differential interferogram phases partially cancels the really strong phase gradients. In the case of co-registration with offset field refinement, the application of the offset field correction "corrects" the azimuth sub-band differential interferometric phases approximately to the differential interferometric phase in the zero Doppler geometry. The split-beam interferograms (SBI) calculated for the co-registered SLCs confirm this: only in the case of co-registration without offset field refinement does the SBI show strong phase differences (Figure 3). Besides the different phases, an important difference is the significantly higher coherence obtained with the offset field refinement co-registration.



(**a**) 20150225 (**b**) 20160601

Figure 1. Azimuth offsets (in SLC pixels) between azimuth sub-band images for the first and last third of the azimuth spectrum. The pixel-level offsets observed for the acquisition on 20160601 are a clear indication for ionospheric effects (dispersive path delay phase gradients along the synthetic aperture causing positional effects).



(**a**) (**b**)

Figure 2. Differential interferograms without (**a**) and with (**b**) offset field refinement in the co-registration step.

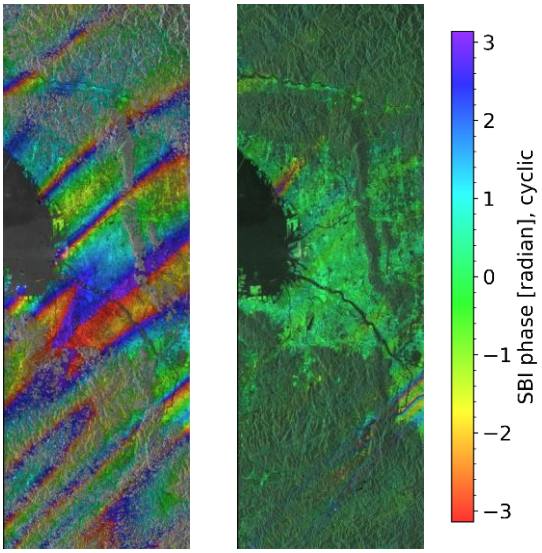


Figure 3. Split-beam interferometric phase obtained for the SLCs co-registered without (**a**) and with (**b**) offset field refinement.

Using the SLCs co-registered with an offset field refinement, we then carried out dispersive phase mitigation. Using Method 1, the unwrapped differential interferogram phase for the main band and the unwrapped double-difference interferogram phase are used (Figure 4). Notice that the phases in the double-difference interferogram are all within the same phase cycle—so unwrapping was trivial. Applying Equation (3) with the scaling factors x and z as listed in Table 1, the dispersive path delay was calculated. Figure 5 shows the PALSAR-3 main band differential interferogram, the estimated dispersive path delay phase and the resulting non-dispersive phase.

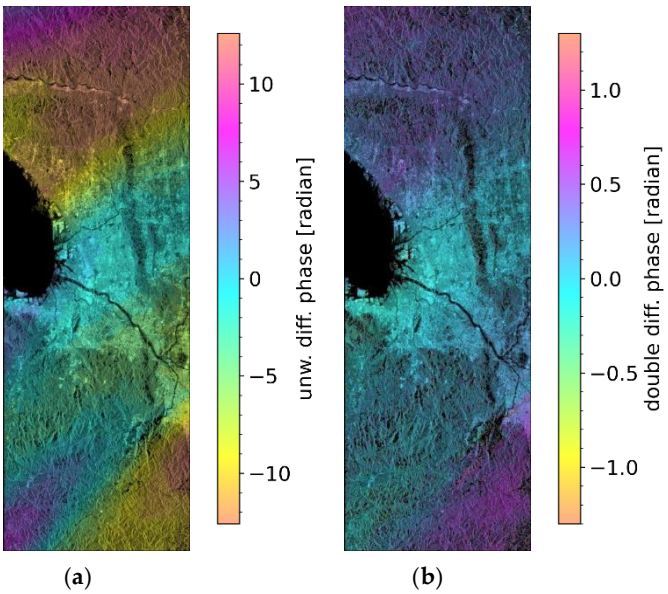


Figure 4. Unwrapped differential interferogram phase for the 28 MHz band data (**a**) and unwrapped double-difference interferogram phase (**b**).

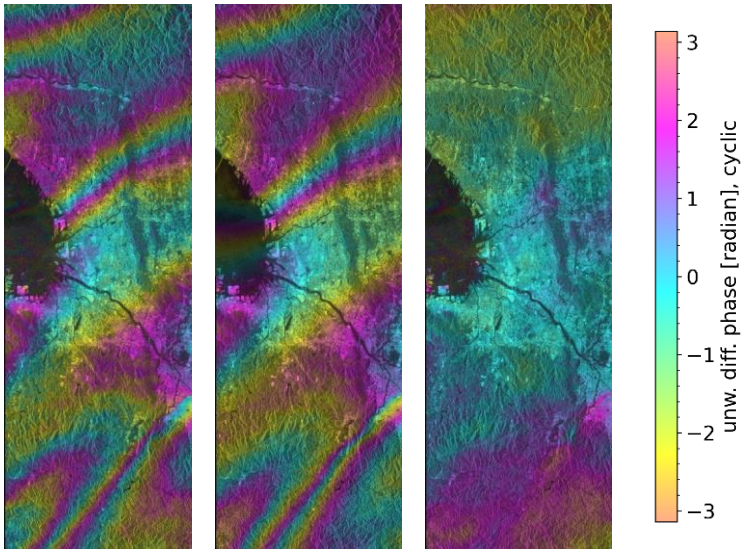


Figure 5. Differential interferogram phase for the 28 MHz band (**a**), estimated dispersive path delay phase (**b**), and non-dispersive or ionosphere-corrected phase (**c**).

Then, we also applied methods M2 and M3. Twice the dispersive path delay phase (Figure 6 left, M2) and twice the non-dispersive phase (Figure 6 right, M3) could be calculated without phase unwrapping, except for the trivial unwrapping of the double-difference interferogram phase.

All three mitigation methods (M1, M2, M3) clearly indicate that the dominant, spatially varying part of the differential interferometric phase corresponds to ionospheric path delay. Considering, the azimuth offset fields (between the two scenes, but also between azimuth sub-bands of a single scene) and SBI tell us that the ionospheric effects are mainly present in the scene acquired on 20160601.

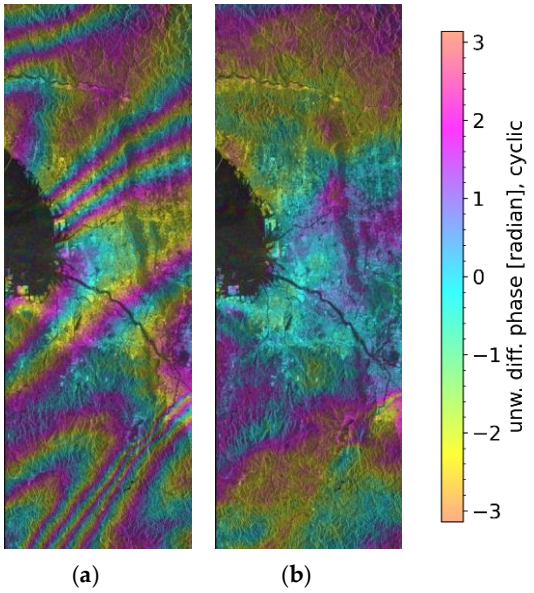


Figure 6. Phase of complex-valued images showing twice the dispersive path delay phase derived using M2 (**a**) and twice the non-dispersive phase derived using M3 (**b**), both calculated without phase unwrapping.

4. Discussion

Checking the simulated PALSAR-3 data for ionospheric effects worked well for the three different methods applied. The calculation of the azimuth offset field between two azimuth sub-bands of a single SLC is a robust process that can be easily automated. An important advantage of this method is that it permits identifying ionospheric distortions in a single SLC. Considering the azimuth offsets of the co-registration offset field refinement also permitted identifying the presence of significant ionospheric effect. This method involves both the reference and the second scene. Consequently, it is not clear which of the two scenes (or both) is affected by ionospheric distortions. Calculating the co-registration refinement offset field is also suited to assess the quality of the co-registration, and it can also be automated easily. More difficult to automate is the conditioning of the refinement offset field (rejecting outliers, spatial filtering, and interpolation) needed to actually refine the co-registration. Using the split-beam interferogram is more delicate. If the SLC co-registration is carried out without offset-field refinement, the SBI phase clearly indicates the presence of ionospheric anomalies. But, if the co-registration is carried out with an offset field refinement the SBI phase is significantly reduced and does not indicate the presence of ionospheric anomalies with the same clarity.

Mitigating the ionospheric effects worked well for the simulated PALSAR-3 data used. Method 1 worked well as we were able to unwrap the differential interferometric phase. In Methods 2 and 3, the complex images for the double dispersive and the double non-dispersive phase could easily be obtained as no unwrapping was required except for the direct conversion of the complex values of the double-difference interferogram to phase values. In cases with extreme ionospheric distortions, the double-difference phases may reach levels outside $(-\pi,\pi)$. In this case, it would be necessary to either unwrap the phase or the level of the values can be reduced by selecting two sub-bands with a reduced spectral separation. In the PALSAR-3 case, this could be achieved by generating two sub-bands of the 28 MHz bandwidth SLC.

Both Methods 2 and 3 should typically be applied. Sometimes, as in the example shown, the ionospheric phase is the dominant phase term. So, unwrapping twice the ionospheric phase will be more challenging than unwrapping the original differential interferogram. Twice the non-dispersive phase, on the other hand, is smoother and clearly simpler to unwrap than the original differential interferogram. In other cases with only small ionospheric distortions, it is exactly the opposite. Twice the dispersive phase will be smoother and therefore more easily unwrapped than the original differential interferogram, that may include substantial displacement phase.

The results obtained for simulated NISAR-L data correspond closely to those obtained for the simulated PALSAR-3 data and are therefore not shown.

5. Conclusions

The upcoming PALSAR-3 and NISAR-L both offer SAR acquisitions in a main frequency band complemented with a narrower secondary frequency band to support the mitigation of ionospheric path delay effects. In preparation of the ionosphere mitigation in PALSAR-3 and NISAR-L data we generalized the mitigation techniques so that they can be applied to data with a single or with two separate frequency bands. Using PALSAR-2 SM1 data with an 80 MHz bandwidth, we simulated PALSAR-3 and NISAR-L SLC data and tested the procedures to identify and mitigate ionospheric path delay effects.

Checking whether ionospheric distortions affect the data can be achieved either for a single SLC or for an interferometric pair. For the investigated data, the presence or absence of significant ionospheric effects, i.e., path delay phase effects and positional effects as a function of the azimuth spectral band, could reliably be identified for the individual SLCs by determining positional offsets between azimuth sub-band images generated using band-pass filtering. The presence of ionospheric distortions could also be identified by calculating the split-beam interferogram, but only if the SLC of the second date was co-

registered to the reference scene without offset field refinement. When applying an offset field refinement in the co-registration, the split-beam interferogram does not clearly show the presence of an ionospheric effects, but azimuth offsets at the SLC pixel level in the refinement offset field clearly indicate the presence of ionospheric effects.

To minimize processing complexity, mitigation method M1 uses the unwrapped phase of the main band differential interferogram and of the double-difference interferogram. The challenging part in the processing is the phase unwrapping step for the differential interferogram. Keeping the scaling factor for this term low, around 0.5, limits the scaling-up of spatial filtering effects and unwrapping errors. Unwrapping the phase of the double-difference interferogram could be performed by directly converting the complex values to phases, as the values were clearly within $[-\pi,\pi]$.

Furthermore, M2 and M3 were successfully used to obtain complex-valued interferograms with the phase corresponding to twice the dispersive phase and twice the non-dispersive phase. The spatial variation of the complex-valued interferogram corresponding to twice the non-dispersive phase was quite smooth, without high gradients (as for the dispersive phase), so unwrapping it is less challenging. The complex-valued interferogram corresponding to twice the dispersive phase clearly confirms the presence of strong ionospheric effects.

Author Contributions: Conceptualization, U.W. and C.W.; methodology, all authors; software, C.W., C.M., and U.W.; validation, U.W. and C.M.; formal analysis, U.W. and O.F.; investigation, all authors; writing—original draft preparation, U.W.; writing—review and editing, O.F. and C.W.; visualization, U.W. and C.M.; supervision, U.W.; project administration, U.W.; funding acquisition, all authors. All authors have read and agreed to the published version of the manuscript.

Funding: This research received no external funding.

Institutional Review Board Statement: Not applicable.

Informed Consent Statement: Not applicable.

Data Availability Statement: Restrictions apply to the availability of these data. The PALSAR-2 SLC data were obtained from JAXA through the research announcement project ER3A4N003.

Acknowledgments: PALSAR-2 original data are copyright JAXA and have been obtained through research announcement project ER3A4N003.

Conflicts of Interest: The authors declare no conflicts of interest.

References

1. Information on PALSAR-3 Instrument. 2023. Available online: https://earth.esa.int/eogateway/documents/20142/2982981/10_191120SARwgcv_tadono.pdf/ee6db1c8-1910-7eed-3661-d25200df3abc (accessed on 27 February 2024).
2. NASA-ISRO SAR (NISAR) Mission Science Users' Handbook. Available online: https://nisar.jpl.nasa.gov/documents/26/NISAR_FINAL_9-6-19.pdf (accessed on 27 February 2024).
3. Bamler, R.; Hartl, P. Synthetic Aperture Radar Interferometry. *Inverse Probl.* **1998**, *14*, R1–R54. https://doi.org/10.1088/0266-5611/14/4/001.
4. Rosen, P.; Hensley, S.; Joughin, I.; Li, F.; Madsen, S.; Rodriguez, E.; Goldstein, R. Synthetic aperture radar interferometry. *Proc. IEEE* **2000**, *88*, 333–382.
5. Zink, M.; Moreira, A. TanDEM-X mission status: The new topography of the earth takes shape. In Proceedings of the 2014 IEEE Geoscience and Remote Sensing Symposium, Quebec City, QC, Canada, 13–18 July 2014; pp. 3386–3389.
6. Massonet, D.; Rossi, M.; Carmona, C.; Adragna, F.; Peltzer, G.; Feigl, K.; Rabaute, T. The displacement field of the Landers earthquake mapped by SAR interferometry. *Nature* **1993**, *364*, 138–142.
7. Sato, H.P.; Harp, E.L. Interpretation of earthquake-induced landslides triggered by the 12 May 2008, M7.9 Wenchuan earthquake in the Beichuan area, Sichuan Province, China, using satellite imagery and Google Earth. *Landslides* **2009**, *6*, 153–159. https://doi.org/10.1007/s10346-009-0147-6.
8. Sandwell, D.; Myer, D.; Mellors, R.; Shimada, M.; Brooks, B.; Foster, J. Accuracy and Resolution of ALOS Interferometry: Vector Deformation Maps of the Father's Day Intrusion at Kilauea. *IEEE Trans. Geosci. Remote Sens.* **2008**, *46*, 3524–3534. https://doi.org/10.1109/TGRS.2008.2000634.
9. Colesanti, C.; Wasowski, J. Investigating landslides with space-borne Synthetic Aperture Radar (SAR) interferometry. *Eng. Geol.* **2006**, *88*, 173–199. https://doi.org/10.1016/j.enggeo.

10. Delacourt, C.; Allemand, P.; Berthier, E.; Raucoules, D.; Casson, B.; Grandjean, P.; Pambrun, C.; Varel, E. Remote-sensing techniques for analysing landslide kinematics: A review. *Bull. Soc. Geol. Fr.* **2007**, *178*, 89–100. https://doi.org/10.2113/gssgfbull.178.2.89.
11. Strozzi, T.; Ambrosi, C.; Raetzo, H. Interpretation of Aerial Photographs and Satellite SAR Interferometry for the Inventory of Landslides. *Remote Sens.* **2013**, *5*, 2554–2570. https://doi.org/10.3390/rs5052554.
12. Joughin, I.; Kwok, R.; Fahnestock, M. Estimation of ice-sheet motion using satellite radar interferometry: Method and error analysis with application to Humboldt Glacier, Greenland. *J. Glaciol.* **1996**, *42*, 564–575.
13. Goldstein, R.M.; Engelhardt, R.; Kamb, B.; Frolich, R. Satellite Radar Interferometry for Monitoring Ice Sheet Motion: Application to an Antarctic Ice Stream. *Science* **1993**, *262*, 1525–1530.
14. Mohr, J.J.; Reeh, N.; Madsen, S.N. Three-dimensional glacial flow and surface elevation measured with radar interferometry. *Nature* **1998**, *391*, 273–276.
15. Gray, A.L.; Mattar, D.E.; Sofko, G. Influence of ionospheric electron density fluctuations on satellite radar interferometry. *Geophys. Res. Lett.* **2000**, *27*, 1451–1454.
16. Meyer, F.; Bamler, R.; Jakowski, N.; Fritz, T.; The potential of low-frequency SAR systems for mapping ionospheric TEC distributions. *IEEE Geosci. Remote Sens. Lett.* **2006**, *3*, 560–564. https://doi.org/10.1109/LGRS.2006.882148.
17. Brcic, R.; Parizzi, A.; Eineder, M.; Bamler, R.; Meyer, F. Estimation and compensation of ionospheric delay for SAR interferometry. In Proceedings of the 2010 IEEE International Geoscience and Remote Sensing Symposium, Honolulu, HI, USA, 25–30 July 2010; pp. 2908–2911.
18. Brcic, R.; Parizzi, A.; Eineder, M.; Bamler, R.; Meyer, F. Ionospheric effects in SAR interferometry: An analysis and comparison of methods for their estimation. In Proceedings of the 2011 IEEE International Geoscience and Remote Sensing Symposium, Vancouver, BC, Canada, 24–29 July 2011; pp. 1497–1500.
19. Rosen, P.A.; Hensley, S.; Chen, C. Measurement and mitigation of the ionosphere in L-band interferometric SAR data. In Proceedings of the 2010 IEEE Radar Conference, Arlington, VA, USA, 10–14 May 2010; pp. 1459–1463.
20. Gomba, G.; De Zan, F. Estimation of ionospheric height variations during an aurora event using multiple semi-focusing levels. In Proceedings of the 2015 IEEE International Geoscience and Remote Sensing Symposium (IGARSS), Milan, Italy, 26–31 July 2015; pp. 4065–4068.
21. Gomba, G.; Parizzi, A.; De Zan, F.; Eineder, M.; Bamler, R. Toward operational compensation of ionospheric effects in SAR interferograms: The split-spectrum method. *IEEE Trans. Geosci. Remote Sens.* **2016**, *54*, 1446–1461.
22. Furuya, M.; Suzuki, T.; Maeda, J.; Heki, K. Midlatitude sporadic-E episodes viewed by L-band split-spectrum InSAR. *Earth Planets Space* **2017**, *69*, 175. https://doi.org/10.1186/s40623-017-0764-6.
23. Liao, H.; Meyer, F.J.; Scheuchl, B.; Mouginot, J.; Joughin, I.; Rignot, E. Ionospheric correction of InSAR data for accurate ice velocity measurement at polar regions. *Remote Sens. Environ.* **2018**, *209*, 166–180. https://doi.org/10.1016/j.rse.2018.02.048.
24. Fattahi, H.; Simons, M.; Agram, P. InSAR Time-Series Estimation of the Ionospheric Phase Delay: An Extension of the Split Range-Spectrum Technique. *IEEE Trans. Geosci. Remote Sens.* **2017**, *55*, 5984–5996. https://doi.org/10.1109/TGRS.2017.2718566.
25. Tymofyeyeva, E.; Fialko, Y. Mitigation of atmospheric phase delays in InSAR data, with application to the eastern California shear zone. *J. Geophys. Res. Solid Earth* **2015**, *120*, 5952–5963. https://doi.org/10.1002/2015JB011886.
26. Wegmüller, U.; Werner, C.; Frey, O.; Magnard, C.; Strozzi, T. Reformulating the Split-Spectrum Method to Facilitate the Estimation and Compensation of the Ionospheric Phase in SAR Interferograms. *Procedia Comput. Sci.* **2018**, *138*, 318–325. https://doi.org/10.1016/j.procs.2018.10.045.
27. Wegmüller, U.; Werner, C.; Strozzi, T.; Wiesmann, A. Ionospheric electron concentration effects on SAR and INSAR. In Proceedings of the 2006 IEEE International Symposium on Geoscience and Remote Sensing, Denver, Colorado, USA, 31 July–4 August 2006.
28. Goldstein, R.M.; Werner, C.L. Radar interferogram filtering for geophysical applications. *Geophys. Res. Lett.* **1998**, *25*, 4035–4038.
29. Gamma Software Information. 2018. Available online: https://www.gamma-rs.ch/software (accessed on 18 January 2024).
30. Costantini, M. A novel phase unwrapping method based on network programming. *IEEE Trans. Geosci. Remote Sens.* **1998**, *36*, 813–818.

Disclaimer/Publisher's Note: The statements, opinions and data contained in all publications are solely those of the individual author(s) and contributor(s) and not of MDPI and/or the editor(s). MDPI and/or the editor(s) disclaim responsibility for any injury to people or property resulting from any ideas, methods, instructions or products referred to in the content.